

## Time-resolved small-angle x-ray scattering measurements of a polymer bicontinuous microemulsion structure factor under shear

Franklin E. Caputo,<sup>1</sup> Wesley R. Burghardt,<sup>1,\*</sup> Kasiraman Krishnan,<sup>2</sup> Frank S. Bates,<sup>2</sup> and Timothy P. Lodge<sup>2,3</sup><sup>1</sup>Department of Chemical Engineering, Northwestern University, Evanston, Illinois 60208<sup>2</sup>Department of Chemical Engineering and Materials Science, University of Minnesota, Minneapolis, Minnesota 55455<sup>3</sup>Department of Chemistry, University of Minnesota, Minneapolis, Minnesota 55455

(Received 29 April 2002; published 21 October 2002)

*In situ* synchrotron x-ray scattering is used in conjunction with a novel annular cone and plate shear cell to study the nonequilibrium structure factor of a polymer bicontinuous microemulsion within the flow-gradient plane. At equilibrium the scattering is well described by the Teubner-Strey structure factor. In steady shear, the structure factor becomes highly anisotropic, owing to loss of scattering intensity along the flow direction and growth of intensity in peaks that progressively rotate towards the velocity-gradient direction. These results contrast with the predictions of a time-dependent Landau-Ginzburg model of Pätzold and Dawson, which generally predicts suppression of scattered intensity. The model assumption of a uniform velocity profile at the microemulsion length scale may be inappropriate owing to high viscosity contrast between the constituents of this sample. While the model anticipates a “stress-x-ray” rule, the data do not support its existence in this system. Nevertheless, strong connections do exist between x-ray anisotropy and stress during transient flow inception experiments. These connections break down upon flow cessation, where stress decays much more rapidly than anisotropy in the structure factor. The mechanical response of this sample exhibits a Rouse-like spectrum of relaxation times, whereas the second moment tensor used to characterize anisotropy in the structure factor exhibits nearly single-exponential relaxation. A phenomenological upper-convected-Maxwell/Lodge model for the second moment tensor provides essentially quantitative predictions of the structural response in step strain and oscillatory shear flow at moderate strains, although additional nonlinearity is found at higher strains.

DOI: 10.1103/PhysRevE.66.041401

PACS number(s): 83.80.Iz, 83.60.Bc, 82.70.Kj, 64.75.+g

### I. INTRODUCTION

Self-assembly processes mediated by amphiphilic interactions in surfactant systems are of intense theoretical and practical interest. Ternary oil-water-surfactant (OWS) mixtures can exhibit a rich array of ordered and disordered fluid phases [1,2]. The surfactant typically occupies the interface between oil-rich and water-rich domains where a subtle balance between energetic interactions and entropic packing considerations determine the interfacial curvature and hence the morphology of the fluid phases. One particularly intriguing structural state is that of a bicontinuous microemulsion [3] featuring a spongelike structure of interpenetrating networks of oil and water with surfactant at the interface. Changes in the relative solubility of the surfactant in the oil and water phases with temperature lead to a characteristic “fish-shaped” isopleth (vertical slice through the ternary phase prism corresponding to a constant ratio of oil-to-water volume fractions) [1,2].

Bates and co-workers have established that suitably designed ternary polymer blends consisting of immiscible homopolymers (*A* and *B*), and their corresponding diblock (*A-B*), also exhibit an equilibrium bicontinuous microemulsion phase [4–8]. Due to the simpler temperature dependence of the thermodynamic interactions in such polymer systems [8],

the isopleth phase diagram is rather simpler than those found in OWS systems. Figure 1 presents an example for the case of a ternary blend of poly(ethyl ethylene) (PEE), poly(dimethyl siloxane) (PDMS), and poly(ethyl ethylene-*b*-dimethyl siloxane) (PEE-PDMS) diblock copolymer [5]. The blend is constructed with  $N_{\text{PEE}} \sim N_{\text{PDMS}}$  and  $N_{\text{PEE-PDMS}} \sim 5N_{\text{PEE}}$ , a condition that assures that the critical temperature of the binary homopolymer blend is comparable to the order-disorder transition temperature of the pure symmetric diblock. This

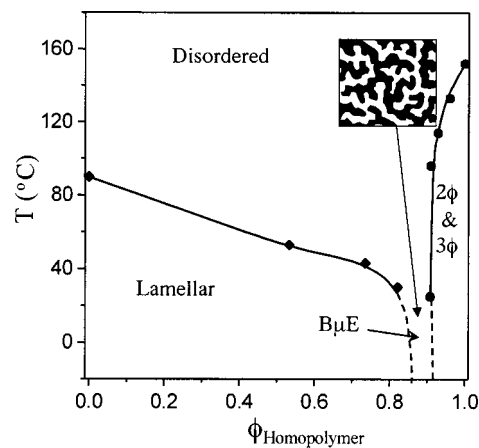


FIG. 1. Isopleth phase diagram for ternary PEE-PDMS system, at constant 1:1 ratio of PEE and PDMS homopolymer [7]. A bicontinuous microemulsion phase exists in a narrow composition channel at total homopolymer concentration of around 90 vol % (inset shows schematic illustration of bicontinuous structure).

\*Corresponding author. Email address: w-burghardt@northwestern.edu

diagram is an isopleth in which the volume fractions of the two homopolymers are equal, and is presented as a function of total homopolymer concentration. At a block copolymer concentration of around 10 vol% (near where mean-field theory predicts an isotropic Lifshitz point [4,9]), a bicontinuous microemulsion phase is found, which is stable over a wide temperature range. This strategy has now been used to create bicontinuous microemulsions in five different ternary blends of the  $A/B/A-B$  type [4,5,7,10], all exhibiting isopleth phase diagrams similar to Fig. 1. More recently, bicontinuous microemulsions have also been found in ternary polymer blends of homopolymers  $A$  and  $B$  with diblock copolymer  $A-C$  [11]. Due to the possibility for different temperature dependence in the  $A-B$  and  $A-C$  interactions, this type of system may be constructed in a way to more closely mimic the “fish” phase diagrams found in OWS systems.

The free energy landscape underlying formation of bicontinuous microemulsion phases was elucidated by Teubner and Strey [12], who demonstrated that only three terms in a Landau-Ginzburg free energy expansion are necessary to capture the essential features observed in neutron and x-ray scattering patterns from microemulsion samples. Their expansion may be written as

$$F(\phi) = a_2\phi^2 + c_1(\nabla\phi)^2 + c_2(\nabla^2\phi)^2, \quad (1)$$

where  $\phi$  is the scalar order parameter. This expression leads to the following form of the equilibrium structure factor measured by scattering [12]:

$$S_0(q) \propto \frac{1}{a_2 + c_1q^2 + c_2q^4}. \quad (2)$$

The Teubner-Strey structure factor, Eq. (2), provides an excellent fit to scattering data on many bicontinuous microemulsions, both in the OWS systems and their more recently discovered polymeric counterparts. The characteristic scattering peak results from values of  $c_1 < 0$ , which corresponds to a system whose free energy, within this phenomenological framework, is lowered by the creation of interface.

Polymers have proved to be exceptionally well-suited model systems for studying microemulsion thermodynamics and dynamics [4–7,10]. This is due to the wide temperature range over which the microemulsion phase is present, and to the slowing of dynamic phenomena relative to OWS systems. While there have been detailed theoretical predictions of linear and nonlinear rheology of microemulsions on the basis of time-dependent Landau-Ginzburg models such as Eq. (1) [13,14], there are very few rheological data available on OWS microemulsions [15,16]. These data show shear thinning in the viscosity, but experiments had to be performed at extremely high shear rates,  $O(10^4) \text{ s}^{-1}$ , due to the rapid structural relaxation.

This paper is a part of an ongoing study of rheology and shear-induced structural changes in a PEE-PDMS polymer bicontinuous microemulsion (i.e., the system of Fig. 1). This microemulsion sample exhibits a wide array of complex rheological and phase behavior under flow. An overview of the phenomena observed in steady shear flow has been given

in Ref. [17]. At low rates (“regime I”) the response is Newtonian, and *in situ* neutron scattering experiments demonstrate negligible perturbation to  $S(\mathbf{q})$ . At somewhat higher rates (“regime II”) the viscosity shows shear thinning, and  $S(\mathbf{q})$  is rendered anisotropic by the flow. A further increase in shear rate leads to more dramatic changes. In “regime III,” the shear stress exhibits a plateau that is independent of shear rate. The sample becomes turbid as a result of a shear-induced transition to a phase-separated state. At still higher shear rates (“regime IV”) stress once again increases with increasing shear rate. Eventually, all vestiges of the original microemulsion scattering peak are eliminated, and the sample behaves essentially like a phase-separated polymer blend under shear. The steady state rheology and structure [18], transient rheology and structure [19], and connections between the quiescent  $S(\mathbf{q})$  and linear viscoelasticity of this sample [20] have all been described.

In this paper, we focus on the nonlinear structural and rheological phenomena *prior* to the onset of bulk phase separation. Although small-angle neutron scattering (SANS) data demonstrate that shear thinning in regime II is associated with deformation of the microemulsion structure [17,18], the available data provide an incomplete picture of the structural changes taking place within the microemulsion. As in most SANS experiments under shear, our earlier studies employed a Couette shear device in which  $S(\mathbf{q})$  is probed only in the flow-vorticity, or  $x$ - $z$ , plane. (Following standard notation, we consider shear flow of the form  $\mathbf{v} = \dot{\gamma}(t)y\mathbf{e}_x$ , so that “ $x$ ” denotes the flow direction, “ $y$ ” denotes the gradient direction, and “ $z$ ” denotes the vorticity or neutral direction.) In sheared complex fluids, the most significant structural changes often take place within the flow-gradient, or  $x$ - $y$ , plane. While a neutron shear cell capable of probing this projection of fluid structure has been constructed by Noirez and Lapp [21], the comparatively long exposure times necessary in neutron scattering limit its applicability to steady state flows. We therefore employ a recently constructed x-ray shear cell modeled after the neutron shear cell of Noirez and Lapp, which allows direct measurements of  $S(\mathbf{q})$  in the  $x$ - $y$  plane [22]. The high flux available at synchrotron sources permits measurements with sufficient time resolution to enable a comprehensive study of transient flow phenomena such as shear inception and cessation, step strain, and oscillatory shear.

## II. EXPERIMENT

### A. Materials

PEE, PDMS, and the corresponding copolymer were synthesized using anionic polymerization; details on the synthesis procedures are available elsewhere [5]. The samples used here have molecular weights of 1710, 2130, and 10 400, respectively, with low polydispersities ( $M_w/M_n \leq 1.1$ ). The diblock copolymer is nearly symmetric;  $f_{\text{PEE}} = 0.52$ . In both homopolymer and copolymer, the PEE was deuterated by saturating the precursor 1,2-polybutadiene with deuterium. The microemulsion sample was prepared with volume composition of 10% copolymer, 45% PEE, and 45% PDMS. Both the molecular weights and volumetric compositions of

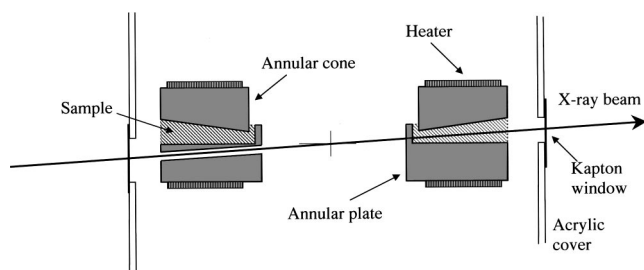


FIG. 2. Schematic representation of annular cone and plate x-ray shear cell. The cone angle is exaggerated in this image; the actual angle is  $5^\circ$ .

this sample render it roughly symmetric in a thermodynamic sense, a condition that facilitates formation of the bicontinuous microemulsion phase [4,9]. However, the sample is very asymmetric dynamically; for instance, at  $20^\circ\text{C}$ , the viscosities of the PEE and PDMS homopolymers are 26 and  $0.026\text{ Pa}\cdot\text{s}$ , respectively [18]. Due to their low molecular weights, the rheology of the pure homopolymer components is Newtonian, with no measurable elasticity in either oscillatory or steady shear.

### B. Mechanical rheometry

Rheological data were obtained primarily with a Rheometrics Scientific ARES controlled strain rheometer, using 50-mm-diameter cone and plate fixtures with a cone angle of  $0.02\text{ rad}$ . A convection oven with liquid nitrogen cooling accessory was used to control temperature to within  $0.1^\circ\text{C}$ ; these measurements were performed under nitrogen atmosphere. Due to the limited normal force sensitivity in this instrument, additional measurements were performed using a Rheometrics fluids spectrometer (RFS) using 50-mm diameter cone and plate fixtures with a cone angle of  $0.04\text{ rad}$  (a larger angle was used to reduce possible squeezing flow artifacts associated with axial compliance). This instrument uses a recirculating water bath for temperature control to within  $0.2^\circ\text{C}$ . Numerous transient experiments were performed under identical conditions using both instruments. The transient shear stress measured by the two rheometers agreed to within a few percent. Reliable normal force data could be obtained on the ARES only in the higher shear rate regions (“regime III and IV”) [19]; all normal force data used in this paper were collected using the RFS.

### C. *In situ* x-ray scattering

The x-ray scattering measurements were performed using a shear cell illustrated schematically in Fig. 2 [22]. The central portions of a traditional cone and plate geometry are removed, creating annular fixtures. The incident x-ray beam is directed through a hole in the fixed lower annular plate, passes through the center of the device at the virtual tip of the cone, and then through the sample between the annular cone and plate on the opposite side of the shear cell. In this way, the beam propagates along the vorticity direction of the shear flow and probes  $S(\mathbf{q})$  in the flow-gradient plane. The

cone angle is  $5^\circ$ . Since the x-ray beam is horizontal, the entire shear cell is mounted on a platform tilted to an angle of  $2.5^\circ$ .

The inner and outer radii of the annular fixtures are 1.5 and 2.5 cm, respectively, giving a path length through the sample of 1 cm. A thin barrier extends upwards from the lower plate at the interior surface to help contain the sample; however, the outer edge is free in order to reduce end effects in the shear flow field. The two fixtures are machined from aluminum, and mounted on ceramic posts to isolate them thermally from other shear cell components. Thin flexible heaters are glued to the faces of the fixtures opposite from the sample, and are driven by a controller that monitors temperature using a thermocouple embedded in the lower plate.

The portion of the shear cell containing the fixtures may be enclosed using clear acrylic covers with Kapton windows for the incident and scattered x-rays. This permits a helium purge to reduce air scattering at small angles, and to cool the sample environment below ambient conditions. The inlet helium gas was cooled by passing it through a length of copper tubing immersed in liquid nitrogen. The electrical heaters then maintained the desired sample temperature by heating against this constant cooling load. We estimate the accuracy of temperature control to be  $\pm 1^\circ\text{C}$ .

The x-ray scattering measurements were performed using beam line 5ID-D, in the DuPont-Northwestern-Dow (DND-CAT) synchrotron research facility at the Advanced Photon Source, Argonne National Laboratory. Radiation with an energy of  $17\text{ keV}$  ( $\lambda = 0.73\text{ \AA}$ ) was selected from an undulator beam using a double-crystal monochromator, and highly collimated using two sets of slits located 32 and 13 m upstream of the sample, each set to a square gap of  $200\text{ }\mu\text{m}$ . A pinhole was placed immediately prior to the shear cell in order to clean up flare from the collimating slits. A vacuum chamber was placed between the shear cell and detector to reduce air scattering. Despite the high collimation of the beam and the vacuum chamber behind the sample, there were several inches of air surrounding the shear cell and upstream of the collimation pinhole, as well as several Kapton windows in the x-ray path. This led to parasitic background scattering that complicates data analysis (see below). Two-dimensional small-angle x-ray scattering (SAXS) images were collected using a charge-coupled device detector (Roper). The detector software has provisions for storing data for a subset of its full active area. This feature enabled us to operate the detector at maximum spatial resolution while reducing the size of data files and, more importantly, increasing the rate at which data could be read and stored to disk. When coupled with the high flux of the undulator source, this enabled us to collect images at a maximum turnover of approximately 0.5 frame/s. Periodically, images were collected using the full active area of the detector to verify that no interesting features (e.g., higher-order reflections from shear-induced ordered phases) were missed.

### D. Representative x-ray patterns and normalization procedures

Figure 3 presents steady state images collected during shear flow of the PEE-PDMS microemulsion at  $15^\circ\text{C}$ . Two

features are evident in these patterns: an isotropic scattering ring that becomes anisotropic upon application of shear and a strong lozenge-shaped feature at lower angles, which does not change significantly as a function of shear rate. We attribute this latter feature to parasitic scattering upstream of the sample, which is masked by the hole in the lower plate through which the beam passes. A small vertical misalignment of the hole axis relative to the beam would explain this shape. Despite this unwelcome complication, these images make clear that shear flow has a significant effect on the microemulsion structure factor. The initially isotropic ring becomes anisotropic, with peaks in scattered intensity that first appear at angles near  $-45^\circ/+135^\circ$  relative to the flow direction and then intensify and rotate towards the velocity-gradient direction.

Quantitative comparisons among scattering patterns require that they first be normalized relative to the incident flux, which varies from one image to another. We have found that the strong air scattering measured in each image frame is an effective surrogate for the incident beam flux. All experiments conducted at a given temperature were normalized in a single block as follows. First, a large number of quiescent patterns was selected. The intensity scale in these images was normalized by an intensity averaged over the low- $q$  regions indicated in Fig. 3(a). Then an additional numerical scaling factor was determined so that the normalized quiescent images gave a scaled intensity equal to 1 at the peak in the microemulsion scattering ring. The same procedures were then applied to all shear flow data collected at that temperature. Since the quiescent scattering intensity changes with temperature, this procedure was repeated separately at each temperature used.

The images in Fig. 3 have all been subjected to this normalization, and are presented using identical false color scales. This helps clarify the important fact that, in certain regions in the  $q_x, q_y$  plane, the structure factor is significantly *larger* than its quiescent value. This contrasts with SANS data collected in the  $q_x, q_z$  plane, where scattering is suppressed along the flow direction while remaining roughly constant along the vorticity direction in regime II [17,18]. Still higher rates (within regime III) lead to a suppression in SANS intensity along both the flow and the vorticity directions, and the emergence of additional low- $q$  scattering associated with the development of shear-induced bulk phase separation [17,18]. Indications of this may be found in Figs. 3(d)–3(f), where a low- $q$  streak perpendicular to the flow direction is superimposed on the parasitic scattering feature. At these higher rates, the intensity of the microemulsion feature also decreases with increasing shear rate, consistent with the neutron scattering observations in regime III [note that the shear stress plateau delineating regime III begins at rates of around  $1 \text{ s}^{-1}$  at  $15^\circ\text{C}$  [17], corresponding to the image in Fig. 3(d)]. Since the low- $q$  scattering significantly overlaps the parasitic scattering, and since we have previously characterized the low- $q$  excess scattering using SANS data [18], we focus here on phenomena at lower rates, below the onset of bulk phase separation, but where shear nevertheless strongly perturbs the structure factor.

To extract compact measures of shear-induced anisotropy from SAXS patterns that are not dominated by the parasitic scattering at small angles, we have adopted a correction procedure outlined schematically in Fig. 4. First, a large number of normalized, quiescent patterns are fit to the Teubner-Strey structure factor, which may be written in scaled form as

$$\hat{S}_0(\hat{q}) = \frac{S_0}{S_{\max}} = \frac{1 - \beta}{\beta \hat{q}^4 - 2\beta \hat{q}^2 + 1}, \quad (3)$$

where  $\hat{q} = q/q_{\max}$  is a scaled scattering vector. In this form, the shape of the structure factor is determined by a single parameter  $\beta = c_1^2/4c_2a_2$ , which is the square of the amphiphilicity factor frequently used to characterize bicontinuous microemulsion thermodynamics [7]. This fitting was performed using quiescent SAXS data along the  $q_y$  direction, since the influence of the parasitic scattering does not extend as far along this axis. The values of  $\beta$  so determined were in excellent agreement with those previously obtained from fitting quiescent SANS data [20]. Figure 4(b) illustrates a normalized Teubner-Strey structure factor that has been fit to many quiescent datasets (of which Fig. 4(a) is a single example). Subtracting the Teubner-Strey fit from each quiescent pattern then leaves a normalized image of the parasitic scattering itself. An *average* parasitic pattern [Fig. 4(c)] was derived by averaging such results from many quiescent scattering patterns. As with the normalization, this procedure was repeated separately at each temperature.

All normalized data collected during shear at a given temperature were corrected by subtracting this normalized parasitic pattern [Fig. 4(d)]. This procedure was reasonably effective; however, the correction was imperfect near the beam stop, and could even lead to anomalous behavior such as negative intensities that would significantly bias subsequent measurements of anisotropy. To reduce the impact of these remaining parasitic effects, a circular region in the center of every corrected image was replaced by the quiescent Teubner-Strey model fit [Fig. 4(e)]. This is purely an *ad hoc* procedure, but it has the virtue that it “fills in” information obscured by the beam stop in addition to removing most of the anisotropic bias inadvertently created by the initial image correction procedure. Despite the fact that the image has undergone considerable manipulation, the result [e.g., Fig. 4(f)] represents a significant improvement and should support a reasonably robust analysis of shear-induced anisotropy.

### III. RESULTS

We first analyze changes in  $S(\mathbf{q})$  under flow using a simple second moment tensor to characterize the degree and direction of shear-induced deformation. These results allow for a critical evaluation of the Landau-Ginzburg model of Pätzold and Dawson [13,14], through a quantitative comparison between computed structure factors and data on the PEE-PDMS microemulsion. Significant differences are found between the model predictions and experiment. We then turn to a survey of transient experiments including shear flow inception, reversal and cessation, step shear strain, and oscillatory shear.

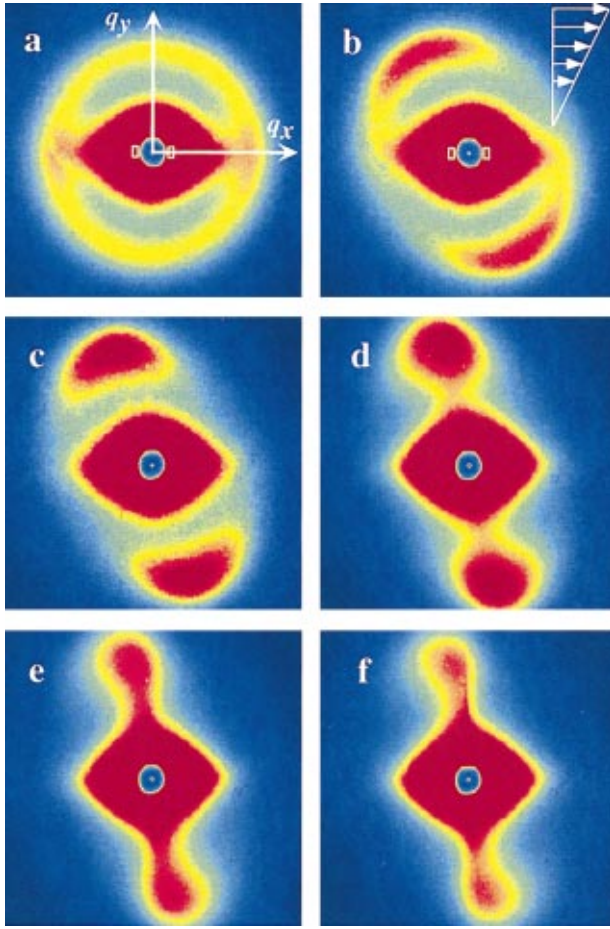


FIG. 3. (Color) Representative steady state SAXS images from PEE-PDMS microemulsion under shear at 15°C and shear rates of (a) 0, (b) 0.1, (c) 0.3, (d) 1.0, (e) 3.0, and (f) 4.0 s<sup>-1</sup>. The lozenge-shaped feature in the center of the pattern is parasitic scattering that passes through the aperture in the shear cell. The intensity scale in all images is normalized such that the peak intensity in the microemulsion scattering pattern in the quiescent state equals unity. Color changes thus directly reflect suppression or enhancement in scattered intensity. The images presented here (and used in analysis) are centered on the incident beam, and cover the range  $|\hat{q}_x|, |\hat{q}_y| \leq 1.5$ . At 15°C,  $q_{\max} = 0.075 \text{ nm}^{-1}$ . Boxes near the beamstop in parts (a) and (b) indicate regions in which parasitic scattering was monitored for normalizing with respect to incident beam flux (see text).

#### A. Steady shear: $S(q)$ and second moment tensor

We characterize the anisotropic scattering by computing a second moment tensor of the dimensionless scattering vector  $\hat{\mathbf{q}}$  weighted by the normalized structure factor:

$$\langle \hat{\mathbf{q}} \hat{\mathbf{q}} \rangle = \int \int \hat{\mathbf{q}} \hat{\mathbf{q}} \hat{S}(\hat{\mathbf{q}}) d\hat{q}_x d\hat{q}_y. \quad (4)$$

Here the integral is carried out over  $|\hat{q}_x, \hat{q}_y| \leq 1.5$  (the range covered by the patterns in Figs. 3 and 4). In the case of an isotropic, quiescent structure factor, this tensor has nonzero diagonal elements given by

$$\langle \hat{q}_x^2 \rangle = \langle \hat{q}_y^2 \rangle = \frac{1}{2} \langle \hat{q}^2 \rangle_0 = \frac{1}{2} \int \int \hat{q}^2 \hat{S}_0(\hat{\mathbf{q}}) d\hat{q}_x d\hat{q}_y, \quad (5)$$

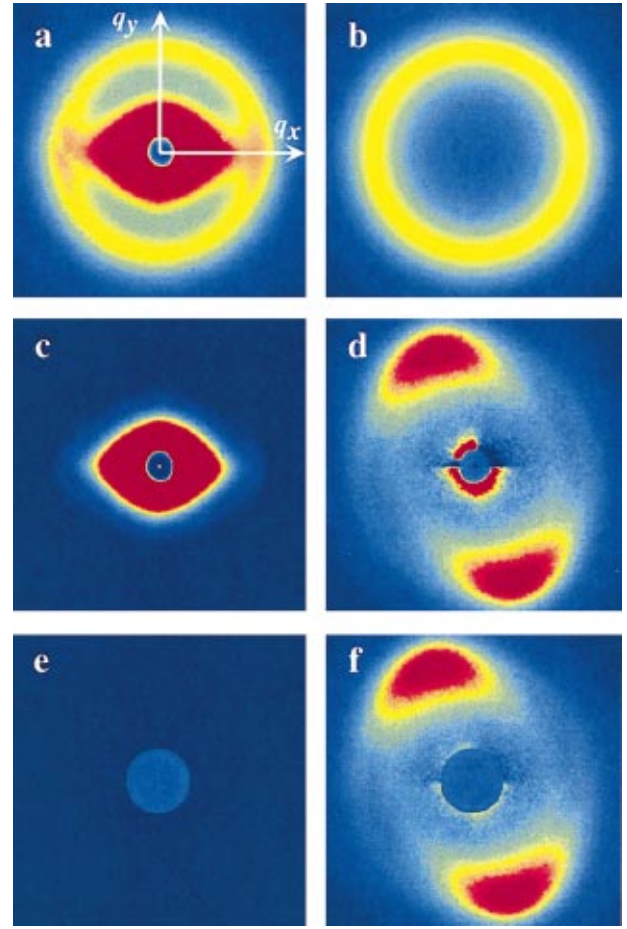


FIG. 4. (Color) Procedure used to correct image for parasitic scattering. For each temperature, a number of normalized quiescent images (a) have been fit to the Teubner-Strey structure factor [Eq. (3)] (b). This is subtracted off to reveal the intrinsic shape of the parasitic scattering (c). Each normalized image obtained under shear flow [for instance, Fig. 3(c), shear rate = 0.3 s<sup>-1</sup>] is corrected by subtracting the parasitic scattering (d). Imperfect correction near the beam stop is accounted for by replacing the central portion of the image with the quiescent Teubner-Strey structure factor appropriate for that temperature (e), leading to the final corrected image (f). Such images are then analyzed using Eqs. (4)–(7) to extract measures of anisotropy and orientation angle.

where  $\hat{S}_0(\hat{\mathbf{q}})$  is given in Eq. (3) above. Finally, we apply one more normalization, dividing the second moment tensor  $\langle \hat{\mathbf{q}} \hat{\mathbf{q}} \rangle$  by  $\frac{1}{2} \langle \hat{q}^2 \rangle_0$ , so that, in the quiescent state, the diagonal components are 1 and the off-diagonal components are 0.

Figure 5 presents the results of this analysis for steady state data collected at 15°C. At the lowest rates the scattering is nearly isotropic. As shear rate increases the off-diagonal element  $\langle \hat{q}_x \hat{q}_y \rangle$  grows in magnitude; due to the enhancement in scattering in the second and fourth quadrants, this quantity is negative. At the same time,  $\langle \hat{q}_y^2 \rangle$  grows and  $\langle \hat{q}_x^2 \rangle$  decreases, leading to anisotropy in the difference of the diagonal elements  $\langle \hat{q}_x^2 \rangle - \langle \hat{q}_y^2 \rangle$  (also a negative quantity).

It is worth noting at this juncture that the excess rheological properties associated with the deformation of the microemulsion structure are predicted to be expressible in terms of

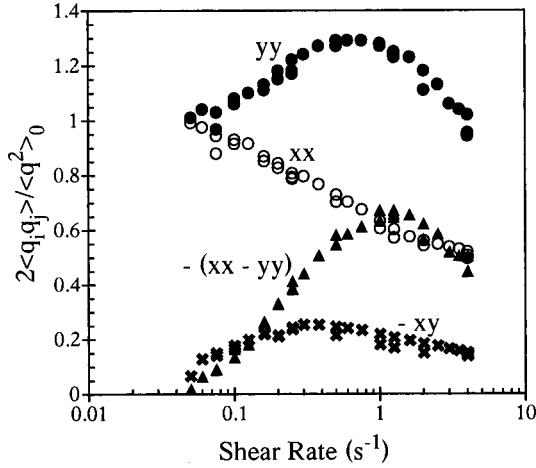


FIG. 5. Normalized second moment tensor components as a function of shear rate in steady shear at 15 °C.

moments of the nonequilibrium structure factor that are very similar to  $\langle \hat{q}_x \hat{q}_y \rangle$  and  $\langle \hat{q}_x^2 \rangle - \langle \hat{q}_y^2 \rangle$  [13,14] (although the rheological properties are expressed in terms of integrals over all of reciprocal space, whereas these measurements are confined to a single slice of reciprocal space with  $q_z=0$ ). In limited cases, we have analyzed the x-ray data using the exact integrands that emerge from the theory [23], but as discussed further below, these more complex analyses do not yield materially different results. In light of this, and recognizing that our experimental data are limited both at the low- $q$  and high- $q$  end, the simpler characterization embodied in Eq. (4) seems sufficient. At the same time, it is reasonable to hope that (and we shall investigate the extent to which) these second moment tensor quantities are related to the bulk rheology. One brief but important example is already apparent in Fig. 5, where  $\langle \hat{q}_x \hat{q}_y \rangle$  exhibits a maximum as a function of shear rate. This agrees with Pätzold and Dawson's prediction of a maximum in the excess microemulsion shear stress as a function of shear rate [14]. We shall return to this specific issue at greater length in subsequent sections.

Another way to characterize anisotropy is via the difference of the eigenvalues of  $\langle \hat{\mathbf{q}} \hat{\mathbf{q}} \rangle$ . When normalized using the quiescent data as described above, this leads to a convenient quantity that we refer to as a “normalized principal anisotropy,”

$$\Delta \equiv \frac{\sqrt{(\langle \hat{q}_x^2 \rangle - \langle \hat{q}_y^2 \rangle)^2 + 4\langle \hat{q}_x \hat{q}_y \rangle^2}}{\frac{1}{2}\langle \hat{q}^2 \rangle_0}. \quad (6)$$

This is complemented by an orientation angle  $\chi$  that defines the rotation of the principal axes of  $\langle \hat{\mathbf{q}} \hat{\mathbf{q}} \rangle$  relative to the flow direction [24]:

$$\chi = \frac{1}{2} \tan^{-1} \left( \frac{2\langle \hat{q}_x \hat{q}_y \rangle}{\langle \hat{q}_x^2 \rangle - \langle \hat{q}_y^2 \rangle} \right). \quad (7)$$

A “shear stress analog”  $\langle \hat{q}_x \hat{q}_y \rangle$  is given by  $\frac{1}{2}\Delta \sin 2\chi$ , and a “first normal stress difference analog”  $\langle \hat{q}_x^2 \rangle - \langle \hat{q}_y^2 \rangle$  is given by  $\Delta \cos 2\chi$  [24]. There are obvious and useful parallels to

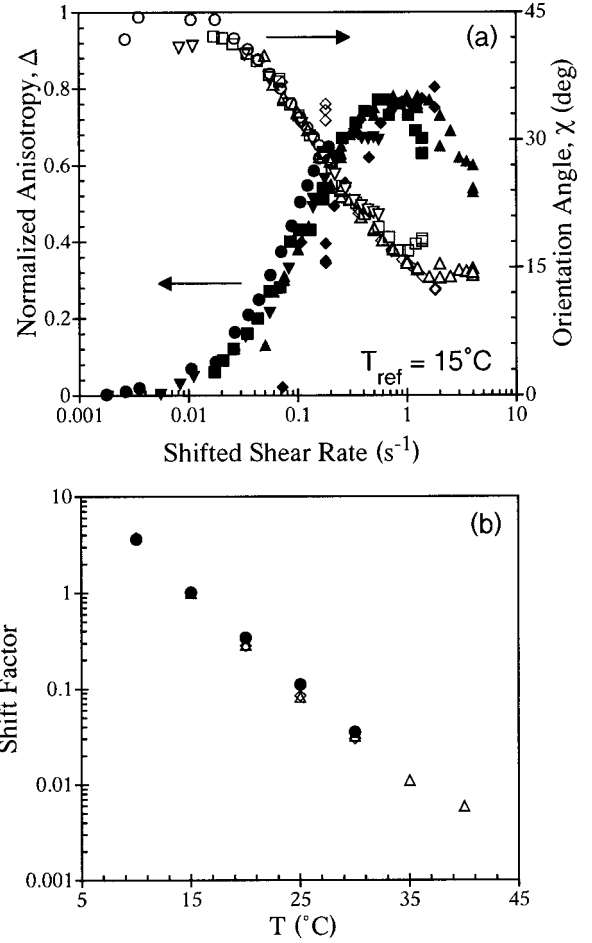


FIG. 6. (a) Normalized principle anisotropy  $\Delta$  (filled symbols) and orientation angle  $\chi$  (open symbols) as a function of reduced shear rate in steady shear experiments conducted at temperatures of 10 (◆, ◇), 15 (▲, △), 20 (■, □), 25 (▼, ▽), and 30 °C (●, ○). Data have been shifted to a reference temperature of 15 °C. (b) Shift factor as a function of temperature (●), compared to shift factors associated with prior rheological measurements of average viscoelastic relaxation time of microemulsion (◇, Ref. [20]), and development of anisotropy in neutron scattering measurements (△, Ref. [18]).

flow birefringence [25]; we will consider the extent to which a “stress-x-ray” law may be valid in this type of complex self-assembled fluid.

Figure 6(a) presents steady state measurements of anisotropy and orientation angle as a function of shear rate at five different temperatures. At each temperature, anisotropy increases with shear rate, but at some point it reaches a maximum and begins to decrease. At the same time the orientation angle decreases with increasing shear rate from a low-rate asymptote of 45°; at high rates it appears that  $\chi$  may reach a limiting value. While temperature has some effect on the details of these data, its major influence is to change the shear rate at which anisotropy develops. In light of the similarity in shape, Fig. 6(a) presents data in reduced form by shifting along the shear rate axis. We performed the shifting using  $\chi$ , although the  $\Delta$  values are also well reduced by this procedure. A similar reduced plot of anisotropy in SANS

data collected within the flow-vorticity plane was presented by Krishnan and co-workers [18]. The interpretation here, as in that case, is that increasing temperature reduces the average relaxation time of the microemulsion so that higher shear rates are required to induce a given degree of anisotropy. Figure 6(b) compares the temperature dependence determined from shifting the x-ray data to that measured from the neutron anisotropy data, as well as to a rheological measure of the average relaxation time of the microemulsion [18]. The agreement is gratifying and establishes that these experiments all probe the same fundamental dynamic phenomena. However, the very strong temperature dependence of the microemulsion relaxation time, and in particular the fact that it is much stronger than the temperature dependence of the zero-shear viscosity, presents a challenge for theoretical predictions of microemulsion rheology [20].

### B. Steady shear: Landau-Ginzburg model predictions

There have been numerous theoretical descriptions of complex fluid structure under shear based on Landau-Ginzburg expansions for the free energy [26–28]. Our measurements of a microemulsion structure factor under shear provide an unusually clear basis for testing the predictions of such models. Here we draw particularly upon the work of Pätzold and Dawson [13,14], who performed a detailed analysis of the effects of shear on the structure factor of microemulsion fluids and the associated rheological behavior. They started with an expansion of the free energy [Eq. (1)] in terms of an order parameter  $\phi$ , which here would be taken to be the local deviation in PEE or PDMS monomer volume fraction from its mean value of 0.5. Their full analysis considered higher-order terms; here, however, we present calculations retaining only the quadratic terms [as in Eq. (1)]. The structure factors computed below are qualitatively very similar to those derived from the more complete theory [14]. Following established procedures, Pätzold and Dawson wrote down a stochastic differential (Langevin) equation for the order parameter field, assuming a linear shear flow:  $\mathbf{v} = \dot{\gamma}(t)y\mathbf{e}_x$  for the convective terms in the equation. This formulation assumes that the macroscopic deformation profile applies at all length scales within the microemulsion, i.e., there is no perturbation to the velocity field associated with local variations in the order parameter.

The equation governing the structure factor under shear may be derived from the Langevin equation. Neglecting the effects of higher-order terms in the free energy expansion, this yields

$$\frac{\partial S(\mathbf{q},t)}{\partial t} + 2\Lambda q^2 K(q)S(\mathbf{q},t) - \dot{\gamma}(t)q_x \frac{\partial S(\mathbf{q},t)}{\partial q_y} = 2\Lambda q^2 T, \quad (8)$$

where  $S(\mathbf{q},t)$  is the structure factor and  $\Lambda$  is a microscopic mobility (Onsager coefficient). This equation is written for the case of a conserved order parameter. The vertex function  $K$  is given by

$$K(q) = c_2 q^4 + c_1 q^2 + a_2. \quad (9)$$

Note that under quiescent conditions, this yields Eq. (2) above for the equilibrium structure factor. It is apparent that, according to Eq. (8), the structure factor is unaffected by the flow if  $q_x = 0$ . This prediction follows directly from the assumption of a uniform velocity gradient in shear.

Here we consider only steady state predictions. By analogy to the experimental analyses described above, Eq. (8) may be written in dimensionless form

$$\frac{d\hat{S}(\hat{\mathbf{q}})}{d\hat{q}_y} = A(\hat{\mathbf{q}})\hat{S}(\hat{\mathbf{q}}) - B(\hat{\mathbf{q}}), \quad (10)$$

where  $A$  and  $B$  are given by

$$A(\hat{\mathbf{q}}) = \frac{\hat{q}^2(1 - 2\beta\hat{q}^2 + \beta\hat{q}^4)}{(1 - \beta)\text{De}\hat{q}_x}, \quad (11)$$

$$B(\hat{\mathbf{q}}) = \frac{\hat{q}^2}{\text{De}\hat{q}_x}. \quad (12)$$

In this expression,  $\text{De}$  is a dimensionless shear rate (Deborah number) defined by

$$\text{De} = \frac{\dot{\gamma}}{2\Lambda a_2(1 - \beta)q_{\max}^2}. \quad (13)$$

(This expression employs the characteristic relaxation time identified by Pätzold and Dawson, Eq. (11) in Ref. [13].)

The first-order ordinary differential equation for  $\hat{S}(\hat{\mathbf{q}})$  may be formally solved using an integrating factor, leading to

$$\begin{aligned} \hat{S}(\hat{\mathbf{q}}) = & - \int_{-\infty}^{\hat{q}_y} d\hat{q}'_y \left( \frac{\hat{q}_x^2 + \hat{q}'_y{}^2}{\text{De}\hat{q}_x} \right) \exp[C(\hat{q}_y - \hat{q}'_y) + D(\hat{q}_y^3 - \hat{q}'_y{}^3) \\ & + E(\hat{q}_y^5 - \hat{q}'_y{}^5) + F(\hat{q}_y^7 - \hat{q}'_y{}^7)], \end{aligned} \quad (14)$$

where

$$C = \frac{\hat{q}_x^2 - 2\beta\hat{q}_x^4 + \beta\hat{q}_x^6}{(1 - \beta)\text{De}\hat{q}_x}, \quad (15)$$

$$D = \frac{3\beta\hat{q}_x^4 - 4\beta\hat{q}_x^2 + 1}{3(1 - \beta)\text{De}\hat{q}_x}, \quad (16)$$

$$E = \frac{3\beta\hat{q}_x^2 - 2\beta}{5(1 - \beta)\text{De}\hat{q}_x}, \quad (17)$$

$$F = \frac{\beta}{7(1 - \beta)\text{De}\hat{q}_x}. \quad (18)$$

The integral in Eq. (14) is performed numerically to compute  $\hat{S}(\hat{\mathbf{q}})$  in the  $(\hat{q}_x, \hat{q}_y)$  plane. As discussed by Pätzold and Dawson [14], this integral is problematic as  $\text{De}\hat{q}_x \rightarrow 0$ ; however, using a fine integration step size, we have had success in computing results down to reasonably small Deborah number.

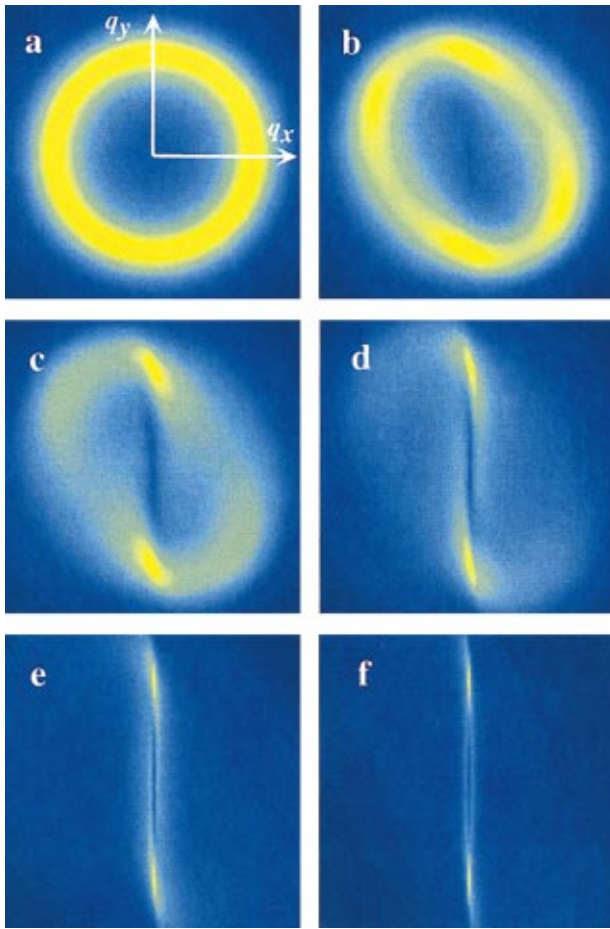


FIG. 7. (Color) Structure factor computed from Landau-Ginzburg model of microemulsion under shear, Eq. (14). Images are computed using the value  $\beta=0.69$  fit to quiescent scattering data at 15 °C, and are presented using the same conventions and color scale as in Fig. 3. Deborah numbers are (a) 0, (b) 0.5, (c) 1.5, (d) 4.5, (e) 13.5, and (f) 40.5.

Figure 7 presents computations of nonequilibrium structure factors for several representative shear rates. These are presented in normalized form over the same dimensionless scattering vector range, and using the same false color scale as the presentation of experimental data in Fig. 3. We note that the qualitative behavior of these structure factors computed using the simplified theory are very similar to those computed by Pätzold and Dawson with the fuller theory [14]. Thus, we feel the simple model provides a sufficient basis for addressing the main issues. While the computed structure factors also become anisotropic under shear, several qualitative features in Figs. 3 and 8 are quite different. An important distinction is the fact that, except for  $q_x=0$ , the theory generally predicts that scattered intensity is *suppressed*. This clearly disagrees with the behavior seen in the experiment, where the emergence of peaks in scattered intensity reflect both a suppression of intensity along the flow direction and an enhancement in scattered intensity at the peak positions.

These differences are further evident when the computed structure factor is subjected to the same second moment tensor analysis used on the experimental data. The second mo-

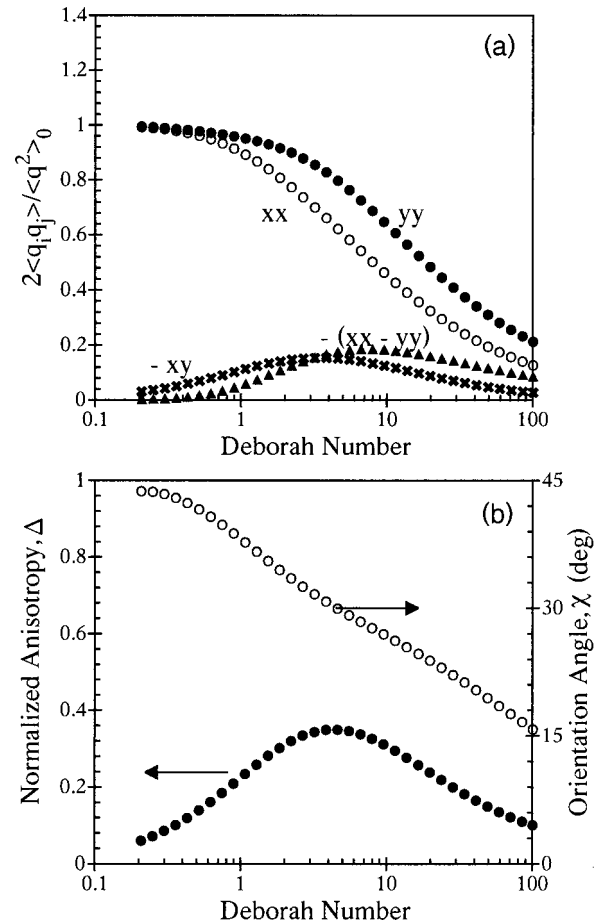


FIG. 8. (a) Normalized second moment tensor components derived from computed structure factors. These may be compared directly against experimental data in Fig. 5. (b) Normalized principal anisotropy  $\Delta$  and orientation angle  $\chi$  derived from computed structure factors. These may be compared directly against experimental data in Fig. 6.

ment tensor is constructed by performing the integral in Eq. (4) over the same limits in the computation as used in the experiments. Together with the normalization procedures described earlier, this assures that these results may be compared *quantitatively* against the experimental results of Figs. 5 and 6 (except for an arbitrary shift along the shear rate axis). Figure 8(a) presents the normalized second moment tensor components analogous to the experimental data in Fig. 5. Many aspects are shared between the data and the model calculation (notably the maximum in  $\langle \hat{q}_x \hat{q}_y \rangle$  with increasing shear rate). The key difference is in the behavior of  $\langle \hat{q}_y^2 \rangle$ . In the computation, both  $\langle \hat{q}_x^2 \rangle$  and  $\langle \hat{q}_y^2 \rangle$  are suppressed by the shear, although to different degrees. In the experiments, however,  $\langle \hat{q}_y^2 \rangle$  initially *increases*, reflecting the enhancement in scattered intensity in the anisotropic microemulsion peak. This has further consequences when comparing  $\Delta$  and  $\chi$  computed from the theoretical structure factors [Fig. 8(b)]. While the predicted behavior is qualitatively similar to that seen in Figs. 5 and 6, in general the theory *underpredicts* the degree of anisotropy and *overpredicts* the orientation angle. Both of these reflect the greater-than-expected first normal stress difference analog found in experiment, traceable again to the enhancement in scattering intensity.

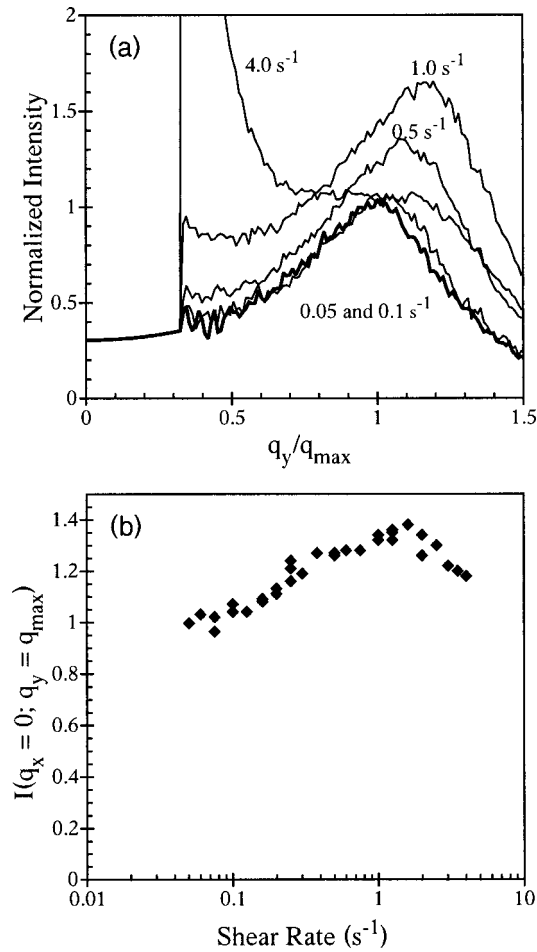


FIG. 9. (a) One-dimensional cuts of experimentally measured normalized structure factor  $\hat{S}(\hat{q}_x=0)$  at several representative shear rates. The data for  $0.05 \text{ s}^{-1}$  (heavy line) are essentially the same as a quiescent pattern. (b) Normalized structure factor  $\hat{S}(\hat{q}_x=0, \hat{q}_y=1)$  as a function of shear rate.

Particularly after comparing Figs. 6(a) and 8(b), one might conclude that, on balance, the theory captures the experimental behavior quite well except for some quantitative discrepancies. However, the x-ray data on the PEE-PDMS microemulsion reveal a fundamental problem in the model formulation. Specifically, having assumed that the local velocity field is unaffected by the microemulsion structure, this theory predicts that there is no change in the structure factor along  $q_x=0$ . Figure 9(a) presents 1D slices of the experimental data along this axis, and makes clear that there are substantial changes in structure factor specifically where the theory says nothing should change. Significantly, these changes occur well within “regime II,” prior to the development of excess low- $q$  scattering associated with the flow-induced bulk phase separation (at rates above  $1 \text{ s}^{-1}$  at this temperature). The scans in Fig. 9(a) are simple vertical pixel scans from the digital images. Due to a small orientation offset in the detector [24], we have also specifically investigated changes in scattering at  $\hat{q}_x=0, \hat{q}_y=1$  [Fig. 9(b)] by computing this exact location on the image using an orientation angle correction factor [24]; the basic conclusions are the same.

The proscription of a uniform velocity field is the logical starting point in developing a model for shear-induced structural changes in microemulsions, and the same assumption has been routinely made in other contexts [26,27]. Given the extreme viscosity contrast between the PEE and PDMS homopolymers under the conditions of these experiments, it would be hard to imagine a more severe test case. However, these results underscore the need to develop more elaborate microscopic descriptions of order-parameter-dependent viscosity and the associated coupling between microstructural evolution and the detailed microscopic velocity profile. Some efforts have been made in this direction in the context of disordered block copolymers [28].

### C. Steady shear: Stress-x-ray law?

As noted above, the second moment tensor  $\langle \hat{q}\hat{q} \rangle$  used to characterize anisotropy in the microemulsion structure factor is quite similar to the structure factor moments used to calculate the excess stress tensor associated with deformation of the microemulsion structure under shear [14]. This suggests the possibility of strong connections between the SAXS data and the rheology of the microemulsion. The strongest such connection would be a “stress-x-ray law”

$$\frac{\Delta}{2} \sin 2\chi = C\sigma, \quad (19a)$$

$$\Delta \cos 2\chi = CN_1, \quad (19b)$$

analogous to the stress-optical law that is widely obeyed in flexible polymers [25], where  $\sigma$  and  $N_1$  are the shear stress and first normal stress difference, respectively, and  $C$  is the “stress-x-ray” coefficient.

Figure 10 presents steady state data collected at  $15^\circ\text{C}$  to test whether or not such a stress x-ray law is suggested for this sample. The shear stress [Fig. 10(a), heavy solid curve] shows three of the four characteristic regimes previously documented in this sample: Newtonian (I), shear thinning (II), and stress plateau (III); the onset of regime IV (where shear stress again increases) is just visible at the highest rates presented in Fig. 10. We have shaded the higher shear rate portions of this figure to emphasize that there is no expectation of a stress-x-ray relation once flow-induced phase separation has occurred. Even with the more sensitive RFS rheometer, reliable  $N_1$  data (star symbols) could only be collected at shear rates of  $0.2 \text{ s}^{-1}$  and above at this temperature, providing a narrow shear rate range within regime II where both shear and normal stress data are available. It appears that  $N_1$  also exhibits a plateau at higher rates [19], although the values decrease slightly across regime III.

The x-ray analogs of shear stress and first normal stress difference are also plotted in Fig. 10(a). Note that both vertical axes span a dynamic range of 200, so the shapes of the x-ray and mechanical data may be sensibly compared. To proceed with more quantitative comparisons, we must first address the fact that any stress-x-ray law would only hold for the “excess” stresses associated with the distortion of the self-assembled fluid structure itself, and not for stresses associated with the shear deformation of the pure components.

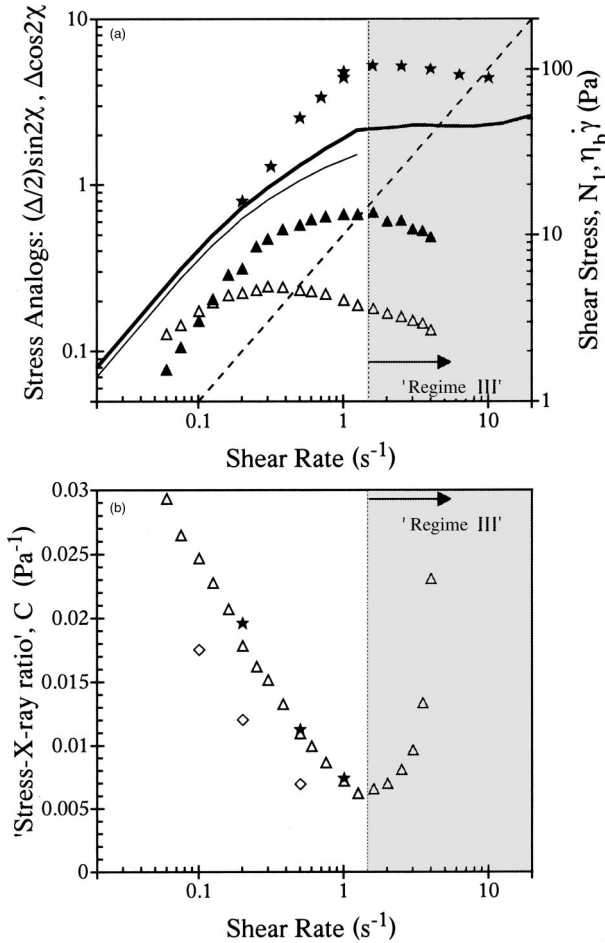


FIG. 10. (a) X-ray stress analogs  $\frac{1}{2}\Delta \sin 2\chi$  ( $\Delta$ ) and  $\Delta \cos 2\chi$  ( $\blacktriangle$ ), left ordinate; and shear stress (heavy solid curve) and first normal stress difference ( $\star$ ), right ordinate, as a function of shear rate in steady shear flow at 15 °C. The dashed line gives viscous stress predicted from the high frequency background viscosity measured in small-amplitude oscillatory shear, and the thin solid line gives the “background-corrected” shear stress  $\sigma - \eta_b \dot{\gamma}$ . (b) “Stress-x-ray ratio” computed from data in part (a). ( $\Delta$ ) Computed using background-corrected shear stress. ( $\star$ ) Computed using first normal stress difference. Also shown are values computed from transient background-corrected shear stress data in flow inception at 10 °C ( $\diamond$ ) [see Fig. 11(b), below].

The situation is analogous to that of flow birefringence measurements in polymer solutions, where the stress-optical law only holds for the polymer contributions to the stress and birefringence, and solvent contributions must first be subtracted. In the present case, however, it is impossible to make independent measurements of the pure component properties, given the complex and rate-dependent morphology of the microemulsion and its temperature-dependent state of mixing. Since the molecular weights of all of the polymer samples are very low, it is reasonable to assume that the pure component stresses are purely viscous in nature; this is definitely true for the two homopolymers. We have previously confronted this issue within an analysis of the linear viscoelasticity of this microemulsion sample [20]. In that work, it was concluded that the limiting viscosity measured at high

frequency (which we dub a “background” viscosity  $\eta_b$ ) provides a reasonable estimate of the purely viscous response of the pure constituents. At 15 °C, this background viscosity was estimated to be 10.0 Pa s [18,20], which accounts for 12% of the total microemulsion zero-shear viscosity.

A simple strategy is to compute a “background-corrected” shear stress according to

$$\sigma_{\text{corr}} = \sigma - \eta_b \dot{\gamma}, \quad (20)$$

where it is assumed that the background viscosity that characterizes the purely viscous dissipation of the pure components in equilibrium oscillatory testing holds also for nonlinear steady shear flow. Figure 10(a) shows that this assumption becomes grossly untenable within regime III, where the estimated “background” stress eventually exceeds the total measured stress. Given that the sample has experienced bulk phase separation in regime III, and that one of these phases may be, in essence, extremely low viscosity PDMS, the failure of Eq. (20) is not surprising. Even within regime II, however, Eq. (20) may be questionable. The structure factors (Fig. 3) show that the sample evolves towards a state in which, crudely speaking, interface whose normal was initially parallel to the flow direction has been rotated towards the gradient direction. This would imply a partial loss of “connectivity” along the gradient direction. Given the very high contrast in viscosity between the PEE and PDMS homopolymers used in this microemulsion, one might easily anticipate that the relative amount of deformation sustained within the PEE- and PDMS-rich “domains” changes as the underlying morphology evolves from the initially undistorted bicontinuous structure towards one whose continuity along the gradient direction is progressively degraded. It is far from clear whether the background viscosity measured under equilibrium conditions remains relevant under these circumstances. However, the only alternative to using Eq. (20) is to simply neglect the background viscosity completely.

Using Eq. (19a), we have computed the stress-x-ray ratio  $C$  using the background-corrected shear stress [Fig. 10(b)]. There is no universal stress-x-ray law in this sample:  $C$  is a strongly decreasing function of shear rate within regime II. At the three shear rates for which both steady  $N_1$  and x-ray data are available, we have also computed the stress-x-ray ratio using Eq. (19b). Although this can only be done for a few points, the normal stress data provide the cleaner test, since the measured  $N_1$  unambiguously reflects only excess microemulsion stresses. The  $C$  values determined from the normal stress data agree very well with those determined from the background-corrected shear stress data. While falling short of a stress-x-ray law, this suggests that there is still a strong geometric connection between the x-ray second moment tensor and the excess stress tensor, and, further, that the correction strategy for the shear stress embodied in Eq. (20) is reasonably sound within regime II.

As noted above, the components of the second moment tensor defined by Eq. (4) differ from the moments of  $S(\mathbf{q})$  that Pätzold and Dawson use to compute stresses in their theory by an additional factor of  $(1 - \hat{q}^2)$  in the integrand of

Eq. (4). Using steady state data at 15 °C, we have reanalyzed data in strict accord with the Pätzold and Dawson stress expressions, and have found that there is no significant qualitative change in behavior from Fig. 10 [23]. In particular, even when the theoretical structure factor moments are used, no stress-x-ray rule exists for this sample.

This discussion has focused only on data collected at 15 °C, since the quantity and quality of available data, both x-ray and mechanical, are highest for this temperature. Fig. 10(b) also includes  $C$  values determined from a more limited consideration of transient background-corrected shear stress and x-ray data collected at 10 °C (see the following section). At this temperature as well,  $C$  decreases significantly with increasing shear rate within regime II.

#### D. Shear flow inception, reversal, and relaxation

Due to a favorable combination of long characteristic relaxation times and the time resolution possible using synchrotron radiation, time-dependent changes in the microemulsion structure factor may readily be measured at lower temperatures. Here we focus exclusively on behavior within regime II; transient rheology and complementary time-resolved small-angle light scattering data in regime III are presented elsewhere [19]. Upon inception of shear flow, the transient response of anisotropy and orientation angle in the microemulsion structure factor is remarkably similar to analogous measurements of birefringence and orientation angle in nonlinear shear flow of conventional polymer liquids [Fig. 11(a)]. Indeed, in light of this similarity it is important to reiterate that the homopolymers contained in this sample are unentangled and Newtonian. The orientation angle starts at 45°, and then drops to a steady state value that depends on the shear rate. At the same time, the anisotropy reaches its steady state value after a mild overshoot. As seen in Fig. 11(a), at short times the initial response scales with the applied shear strain.

The similarity to the nonlinear rheology of polymers extends to the x-ray stress analogs, as well. Figure 11(b) presents the shear stress analog  $\frac{1}{2}\Delta \sin 2\chi$  converted to a stress using the (rate-dependent)  $C$  values presented in Fig. 10(b). Although this sample does not obey a stress-x-ray law in a strict sense, there is remarkable agreement in the transient shear stress and x-ray shear stress analog once their steady state values have been reconciled. With increasing shear rate, the transient behavior evolves from a monotonic growth in shear stress (which follows the linear viscoelastic limit at sufficiently low rate [19]) to a large shear stress overshoot. Reliable transient  $N_1$  data are much more difficult to obtain, but Fig. 11(c) demonstrates that the connection between normal stress and its x-ray analog is also strong. Here the mechanical data are rather noisier than the x-ray data; however, it appears that  $N_1$  also exhibits a transient overshoot at higher rates within regime II.

Figure 12 presents mechanical and x-ray data obtained upon reversal of shear flow direction in terms of shear stress and its x-ray analog. This experiment reveals a breakdown in the close connection between the x-ray and mechanical response. There is a significant discrepancy at short times,

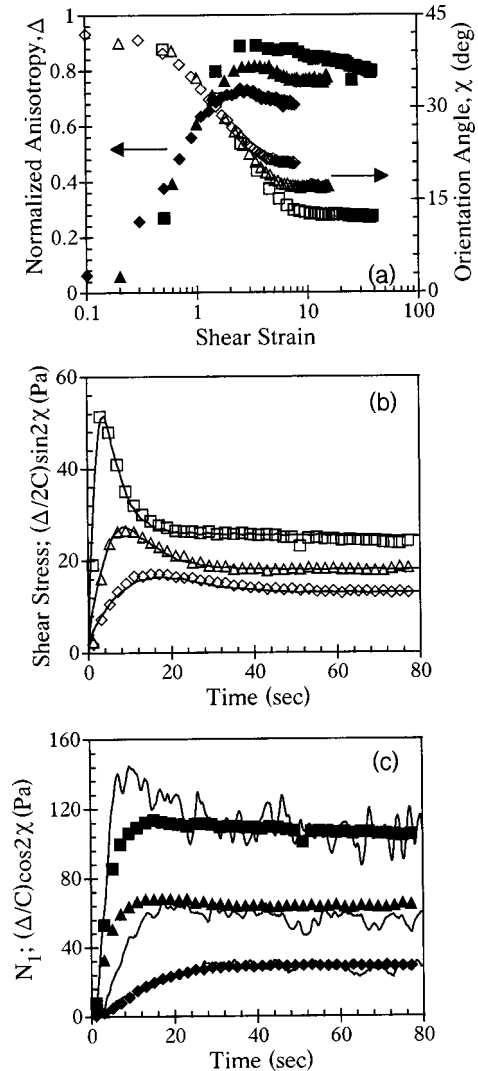


FIG. 11. Transient data during shear inception at 10 °C and rates of 0.1 ( $\blacklozenge, \diamond$ ), 0.2 ( $\blacktriangle, \triangle$ ), and 0.5  $s^{-1}$  ( $\blacksquare, \square$ ). (a) Normalized principal anisotropy  $\Delta$  (filled symbols) and orientation angle  $\chi$  (open symbols) vs applied strain. (b) Comparison between transient behavior of “background-corrected” shear stress  $\sigma - \eta_b \dot{\gamma}$  (solid lines) and x-ray shear stress analog (symbols). (c) Comparison between transient behavior of first normal stress difference  $N_1$  (solid lines) and x-ray  $N_1$  analog (symbols). Values of  $C$  are given in Fig. 10 above.

where the shear stress changes sign in response to the flow reversal much more rapidly than the corresponding component of the x-ray second moment tensor.

Upon cessation of shear flow, the normalized principal anisotropy exhibits nearly single-exponential decay, while the orientation angle remains more or less constant at its prior steady state value [Fig. 13(a)]. This provides an interesting departure from the analogy with flexible polymer birefringence, where the orientation angle typically evolves towards a smaller value during the relaxation. In polymers, this is associated with the distribution of relaxation times. Given the single-exponential relaxation of  $\Delta$ , a constant value of  $\chi$  during the relaxation is expected.

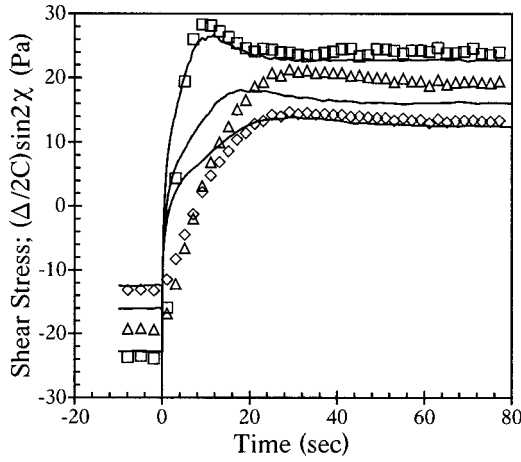


FIG. 12. Comparison between transient behavior of “background-corrected” shear stress  $\sigma - \eta_b \dot{\gamma}$  (solid lines) and x-ray shear stress analog (symbols) following shear flow reversal at 10 °C. Shear rates are 0.1 ( $\diamond$ ), 0.2 ( $\triangle$ ), and 0.5  $\text{s}^{-1}$  ( $\square$ ). Values of  $C$  are given in Fig. 10 above.

The relaxation data also provide a significant contrast when compared with mechanical data [Fig. 13(b)]. The x-ray shear stress analog shows essentially the same single-exponential relaxation that would be anticipated from Fig. 13(a). However, the shear stress (smooth curves) exhibits a rapid initial drop before ultimately relaxing with a slowest relaxation time comparable to that which governs the relaxation of x-ray anisotropy. It is important to recognize that this rapid drop in stress is *not* associated with the viscous background stresses alluded to earlier. All of the comparisons in Figs. 11–13 have used background-corrected stress data and the corresponding background-corrected  $C$  values from Fig. 10. During the prior steady state [Fig. 11(b)], and at the shortest times for which mechanical shear stress data may be obtained during relaxation ( $\sim 0.01$ – $0.1$  s), the shear stress and its x-ray analog agree well. This initial drop in shear stress, while poorly resolved on the linear time scale in Fig. 13(b), occurs well within the time resolution of these mechanical measurements and is too slow to be attributed to viscous effects. Comparing Figs. 11(b) and 13(b), it is clear that there are very different relationships between the x-ray second moment tensor and the stress tensor during shear flow inception and relaxation. At present we offer no explanation for this. It is interesting to note, however, a superficial similarity between this behavior and the spectacular stress-optical failure in dilute polymer solutions in strong transient flows known as “stress-birefringence hysteresis” [29]. A final intriguing aspect of Fig. 13(b) is how, after a short time, the shear stress becomes nearly independent of the previously applied shear rate, while the x-ray data remain vertically shifted throughout the relaxation process according to their prior degree of anisotropy during steady shear.

#### E. Step strain and oscillatory shear flow: Experiment and phenomenological modeling

We now turn to step strain deformations. As would be anticipated from the steady shear relaxation data, anisotropy

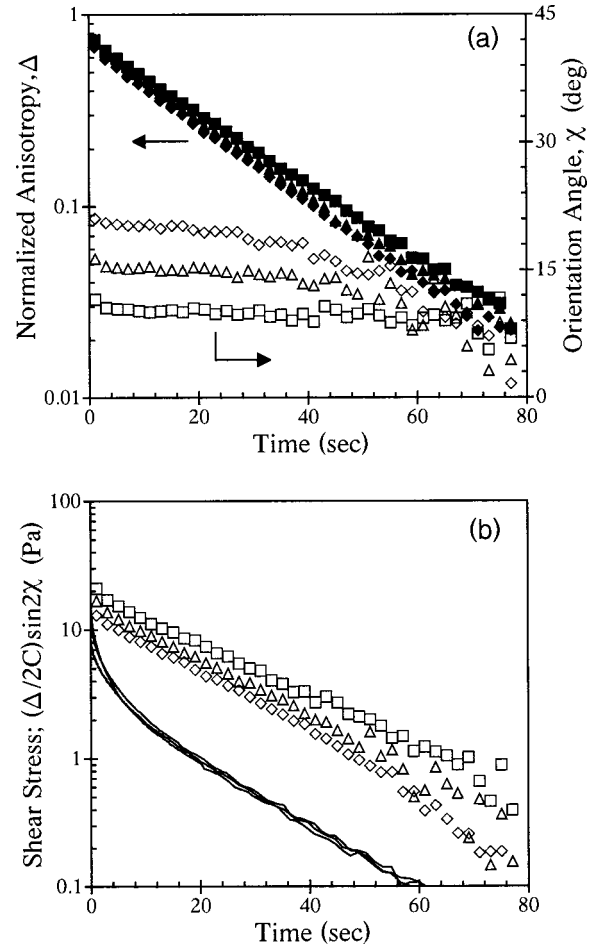


FIG. 13. Transient data following shear flow cessation at 10 °C and rates of 0.1 ( $\diamond, \diamond$ ), 0.2 ( $\blacktriangle, \triangle$ ), and 0.5  $\text{s}^{-1}$  ( $\blacksquare, \square$ ). (a) Normalized principal anisotropy  $\Delta$  (filled symbols) and orientation angle  $\chi$  (open symbols) vs time. (b) Comparison between transient behavior of shear stress (solid lines) and x-ray shear stress analog (symbols) following shear flow cessation. Values of  $C$  are given in Fig. 10 above.

relaxes in an essentially single-exponential decay following step strain, while the orientation angle remains nearly constant [Fig. 14(a)]. The behavior of  $\chi$  indicates that the shear stress and  $N_1$  x-ray analogs both relax at the same rate. The orientation angle decreases as applied strain increases; models that invoke an affine deformation of microstructure make the following prediction for orientation angle following a step strain deformation:

$$\chi = \frac{1}{2} \tan^{-1} \left( \frac{2}{\gamma_0} \right), \quad (21)$$

where  $\gamma_0$  is the magnitude of the applied strain. This relationship is seen to hold for the microemulsion [Fig. 14(b)]. This is equivalent to noting that the x-ray analogs of shear stress and  $N_1$  obey the Lodge-Meissner relation [30].

Figure 15(a) considers the shear stress analog in greater detail. As anticipated from Fig. 14, it obeys a single-exponential relaxation that may be expressed as

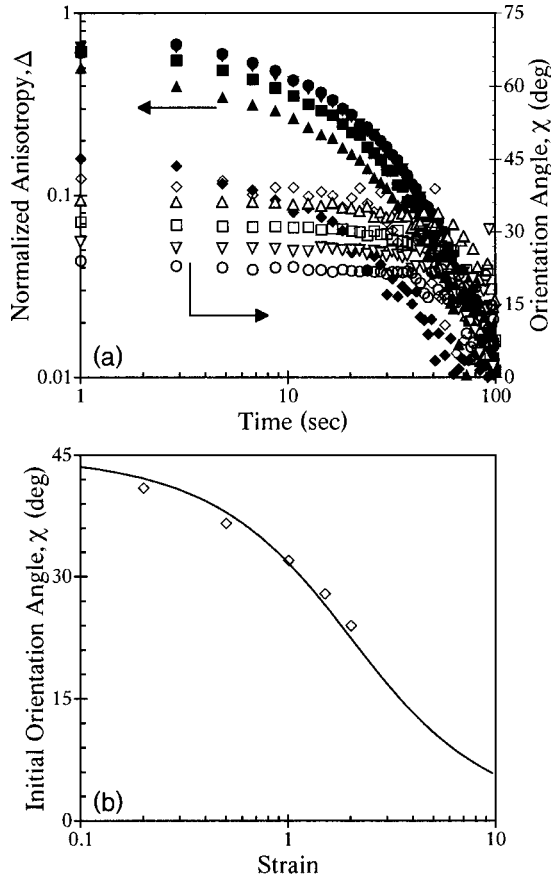


FIG. 14. Response of microemulsion structure factor to step strain deformation at 10 °C. (a) Normalized principal anisotropy  $\Delta$  (closed symbols) and orientation angle  $\chi$  (open symbols) vs time following step strain of magnitude 20% ( $\blacklozenge, \diamond$ ), 50% ( $\blacktriangle, \triangle$ ), 100% ( $\blacksquare, \square$ ), 150% ( $\blacktriangledown, \triangledown$ ), and 200% ( $\bullet, \circ$ ). (b) Initial orientation angle as a function of applied strain; solid curve represents predictions for affine deformation [Eq. (21)].

$$\frac{\Delta}{2} \sin 2\chi = \gamma_0 \mathcal{G}(t) = \gamma_0 \mathcal{G} \exp(-t/\tau), \quad (22)$$

where  $\mathcal{G}(t)$  is a relaxation modulus analog, taken here to be a single-exponential function characterized by an “x-ray anisotropy modulus”  $\mathcal{G}$  and a relaxation time  $\tau$ . All of the data in Fig. 15(a) are well represented using a value  $\tau=20$  s, and obey time-strain factorability. The strain-dependent values of  $\mathcal{G}$  determined by fitting Eq. (22) to the data are presented in Fig. 15(b). By analogy to conventional rheology, it is reasonable to expect a regime of linear response in which  $\mathcal{G}$  is independent of strain, followed by a nonlinear regime at higher strains. Due to the restricted number of strain values used in these experiments, it is not clear if or where a linear regime exists. The modulus  $\mathcal{G}$  initially increases somewhat as strain increases from 20% to 50%, and then drops more dramatically at higher strains.

Data presented here and in the preceding section convincingly show that the anisotropy in the structure factor probed in these SAXS experiments, at least as characterized by the second moment tensor [Eq. (4)], exhibits robust single-exponential relaxation. This is in interesting contrast to linear

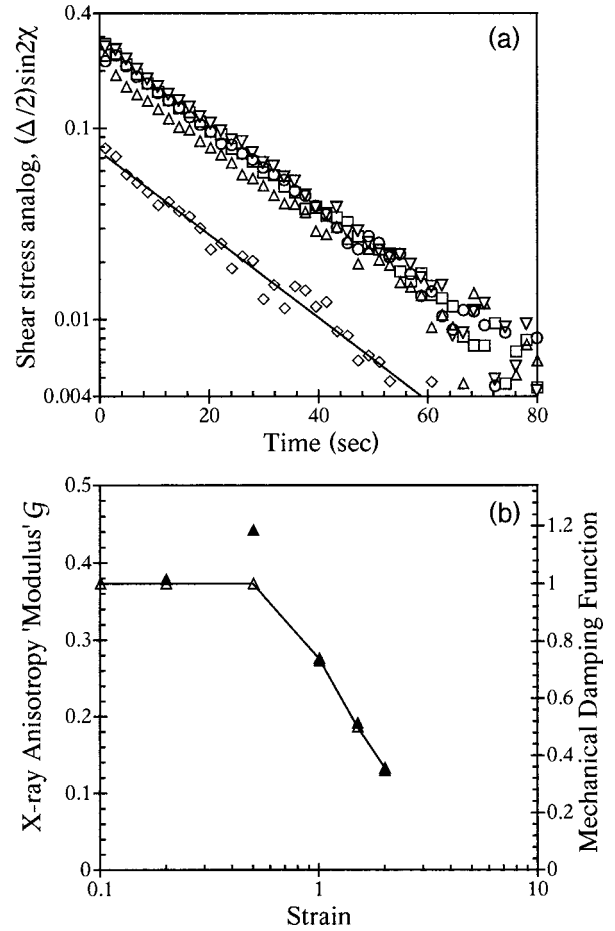


FIG. 15. (a) X-ray shear stress analog following step strain deformation of magnitude 20% ( $\diamond$ ), 50% ( $\triangle$ ), 100% ( $\square$ ), 150% ( $\triangledown$ ), and 200% ( $\circ$ ) at 10 °C. Solid line represents single-exponential predictions of Eq. (22) using  $\mathcal{G}=0.378$  and  $\tau=20$  s. (b) X-ray modulus analog  $\mathcal{G}$  ( $\blacktriangle$ ) as a function of applied strain, based on step strain measurements at 10 °C. Also presented is the shear stress damping function ( $\triangle$ , line) derived from mechanical step strain experiments at 10 °C [19].

viscoelastic rheological data for this microemulsion, which exhibit a Rouse-like spectrum of relaxation times [20], in qualitative agreement with the predictions of Pätzold and Dawson [14]. The step strain relaxation data also show time-strain factorability, where the time dependence is in good agreement with oscillatory shear data [19] (that is, there is a spectrum of relaxation times for shear stress relaxation following a step strain). It is thus clear that here, as in Fig. 13(b), there will be significant deviations from any hypothetical stress-x-ray law. The strain dependence of the mechanical step strain data is reproduced in Fig. 15(b) in terms of the damping function

$$h(\gamma_0) = \frac{G(t, \gamma_0)}{G(t)}. \quad (23)$$

In mechanical testing, the response is linear to strains of 50%, and then shows strain-softening behavior at higher strains [19]. Adjusting the scales of the vertical axes in Fig.

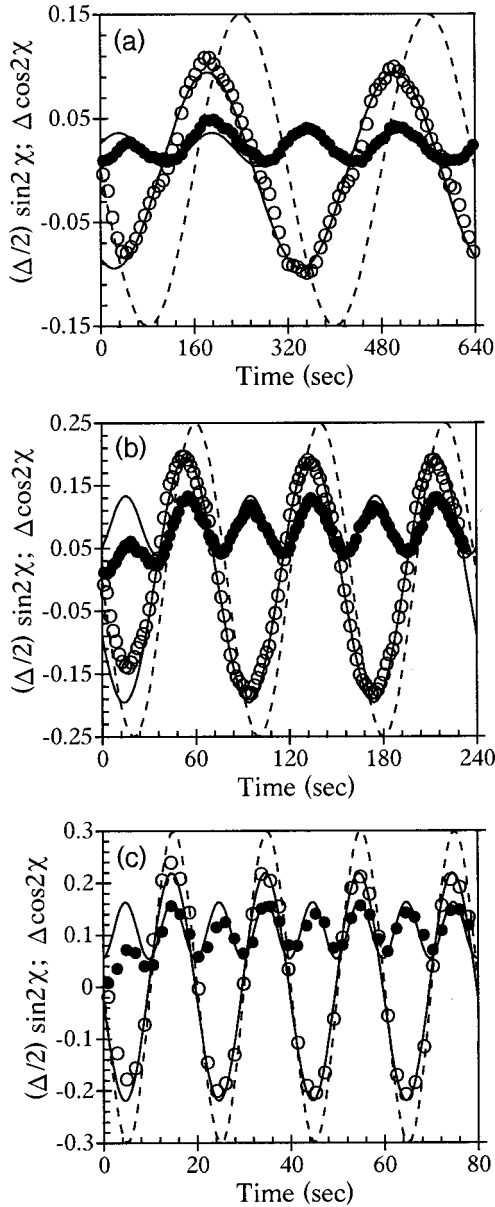


FIG. 16. Response of microemulsion structure factor to oscillatory shear deformation at 10 °C and 50% strain. X-ray shear stress analog  $\frac{1}{2}\Delta \sin 2\chi$  (○), first normal stress difference analog  $\Delta \cos 2\chi$  (●), and input strain wave (dashed curve) as a function of time. (a)  $f=0.003$  125 Hz. (b)  $f=0.0125$  Hz. (c)  $f=0.05$  Hz. Solid curves through data are predictions of phenomenological model [Eq. (26)] as described in the text.

15(b), we find that the strain dependences of the shear stress and its x-ray analog are similar overall, provided one assumes that the x-ray data at 20% strain are within the linear response regime. Interestingly, however, the mechanical data do not show the mild strain-hardening behavior suggested in the x-ray results [31]. The origin of this discrepancy is not known.

We have also subjected the microemulsion sample to oscillatory shear over a range of frequencies and strains. Figure 16 shows representative results at 50% strain (the smallest strain for which oscillatory testing was performed), in terms

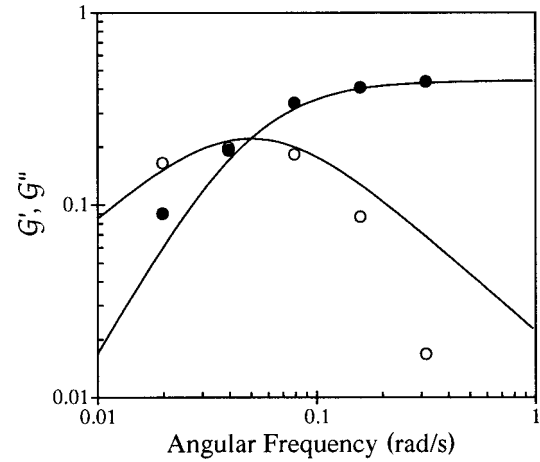


FIG. 17. X-ray analogs of storage and loss moduli  $\mathcal{G}'$  (●) and  $\mathcal{G}''$  (○), measured during oscillatory shear at 10 °C and 50% strain. Solid curves present predictions of Eqs. (24) and (25) using  $\mathcal{G}=0.442$  and  $\tau=20$  s, determined from step strain at 50% strain. (The data may be more accurately fit using  $\mathcal{G}=0.442$  and  $\tau=24$  s.)

of the time-dependent shear stress and  $N_1$  analogs. The response is, overall, very similar to that expected for a viscoelastic fluid. The shear stress analog oscillates at the input frequency, but with a phase and amplitude that vary with the frequency used. At low frequencies, there is a significant phase difference between the applied strain and the resulting shear stress analog, while at the highest frequency the phase angle is very small (the dashed lines in Fig. 16 represent the input strain wave form). This is an interesting contrast, directly related to the single-exponential relaxation of the x-ray anisotropy, to the mechanical results that asymptote at a phase angle near 45° at high frequency [20]. The  $N_1$  analog oscillates around a nonzero mean at twice the applied frequency.

The time-dependent shear stress analog may be resolved into components in phase and out of phase with the applied strain. If  $\gamma(t) = \gamma_0 \sin \omega t$ , and assuming a linear response, then

$$\frac{\Delta}{2} \sin 2\chi = \gamma_0 [\mathcal{G}'(\omega) \sin \omega t + \mathcal{G}''(\omega) \cos \omega t]. \quad (24)$$

For single-exponential relaxation [Eq. (22)], the “x-ray storage and loss moduli” are given by

$$\mathcal{G}'(\omega) = \frac{\mathcal{G}\omega^2\tau^2}{1 + \omega^2\tau^2}, \quad \mathcal{G}''(\omega) = \frac{\mathcal{G}\omega\tau}{1 + \omega^2\tau^2}. \quad (25)$$

The in-phase and out-of-phase components of the x-ray shear stress analog were extracted from data, like those in Fig. 16, using cross correlation (only using data after the initial transient period). Figure 17 shows that the modulus and relaxation time determined from step strain data at 50% strain provide for a reasonable prediction of the oscillatory response using Eqs. (24) and (25). Thus, it appears that 50% strain is small enough to yield a nearly linear response, Fig. 15(b) notwithstanding.

To analyze the time-dependent normal stress analog in greater detail, we consider the following phenomenological model for the doubly normalized second moment tensor, in the form of an upper-convected Maxwell (UCM) or Lodge equation [32]:

$$\frac{\langle \hat{\mathbf{q}}\hat{\mathbf{q}} \rangle}{\frac{1}{2} \langle \hat{q}^2 \rangle_0} + \tau \frac{\overset{\nabla}{\langle \hat{\mathbf{q}}\hat{\mathbf{q}} \rangle}}{\frac{1}{2} \langle \hat{q}^2 \rangle_0} = 2\mathcal{G}\tau\mathbf{D}, \quad (26)$$

where  $\mathcal{G}$  is a “modulus,”  $\tau$  is a relaxation time,  $\mathbf{D}$  is the rate of deformation tensor, and superscript “ $\nabla$ ” denotes an upper-convected time derivative. This model reproduces the single-exponential step strain predictions [Eq. (22)], while also predicting the existence of a normal stress analog such that Eq. (21) is satisfied (in other words, it predicts the Lodge-Meissner relation). In oscillation, the shear stress analog predictions are the same as those given above in Eqs. (24) and (25), while it also predicts the existence of normal components given by

$$\Delta \cos 2\chi = \mathcal{G}'(\omega) \gamma_0^2 \left[ 1 + \frac{3\omega^2\tau^2}{1+4\omega^2\tau^2} \sin 2\omega t + \frac{1-2\omega^2\tau^2}{1+4\omega^2\tau^2} \cos 2\omega t \right]. \quad (27)$$

(Note that this equation, like Eq. (24) above, neglects the initial transient during the startup of oscillatory shear.) While this UCM-like model predicts nonlinear phenomena such as the existence of normal components of  $\langle \hat{\mathbf{q}}\hat{\mathbf{q}} \rangle$ , it cannot predict nonlinearity in its shear “stress” response; hence we restrict its use to the data collected at the smallest strain of 50%, which is apparently already somewhat outside the linear range. As in Fig. 17, we use the “modulus” value measured in step strain. However, noting that the data in Fig. 17 could be more faithfully described using a slightly modified relaxation time of 24 s, we use this value here. Figure 16 includes predictions of Eq. (26) for shear stress and  $N_1$  x-ray analogs in oscillatory shear, drawn as solid lines. After the initial transient period, this phenomenological model provides essentially quantitative predictions of the time-dependent x-ray data at this moderate strain level.

We have collected similar oscillatory datasets at larger strains of 100% and 200%; Figs. 18(a)–18(c) present illustrative data at three frequencies for experiments at a strain amplitude of 200%. The larger strain leads to (i) larger anisotropy overall and a larger  $N_1$  analog in particular, and (ii) visible nonlinear effects in the shapes of the wave forms, which are no longer sinusoidal. It might be interesting to continue to explore the relationships among the data collected in these various nonlinear transient flows by extending the modeling to incorporate more substantial nonlinearities in the formulation of a phenomenological anisotropy model. Given the time-strain factorability observed in step strain, a Wagner-type integral model [33] would be a logical starting point, although it would require formulating a damping function that could account for both the moderate strain-hardening and subsequent strain-softening behavior seen in Fig. 15(b). A more satisfying use of these transient data would be as a platform for testing the transient predictions of more sophisticated theories such as that of Pätzold and Dawson [13,14]. In light of the deficiencies described above regarding the steady state predictions of this particular theory, however, it appears that detailed comparisons between these transient data and theory are perhaps best postponed until

such theories are refined to the point where they can provide a more accurate portrayal of steady state.

#### IV. DISCUSSION

These SAXS and rheology data provide an opportunity to explore detailed connections between flow-induced structural changes and rheology in an interesting complex fluid, the bicontinuous microemulsion phase in  $A/B/A-B$  ternary polymer blends. Available theory [13,14] suggests that knowledge of the nonequilibrium structure factor should be sufficient to predict the stresses. We have previously demonstrated that this theory describes the qualitative aspects of the linear viscoelasticity quite satisfactorily, but that there are significant quantitative discrepancies [20]. Results presented here suggest that, not surprisingly, the data in the nonlinear regime provide an even more stringent test of this type of theory.

Two major difficulties are revealed. First, the qualitative response of the structure factor (Fig. 3) is plainly different from the predictions of the theory (Fig. 7). This is almost certainly due in part to the fact that this particular sample should have a highly concentration-dependent viscosity that would certainly impact the local velocity profile on the length scale of the concentration fluctuations. Conversely, the theory postulates a uniform shear profile at all length scales. The results in Fig. 9 seem definitive in at least this respect: the assumption of a linear shear profile at the microemulsion length scale is inappropriate in this sample. However, it is also plausible that the physical picture of a single, fluctuating order parameter implicit in the Teubner-Strey model [Eq. (1)] cannot adequately describe the detailed local structure and dynamics of three-component materials in which an amphiphile is strongly confined to an interface. The “smearing out” of scattered intensity in the predictions of Fig. 7 is perfectly sensible within the model, but hard to reconcile with a molecular-scale picture. Conversely, the experimental structure factor measurements (Fig. 3) strongly suggest that interface is, in some crude sense, conserved and

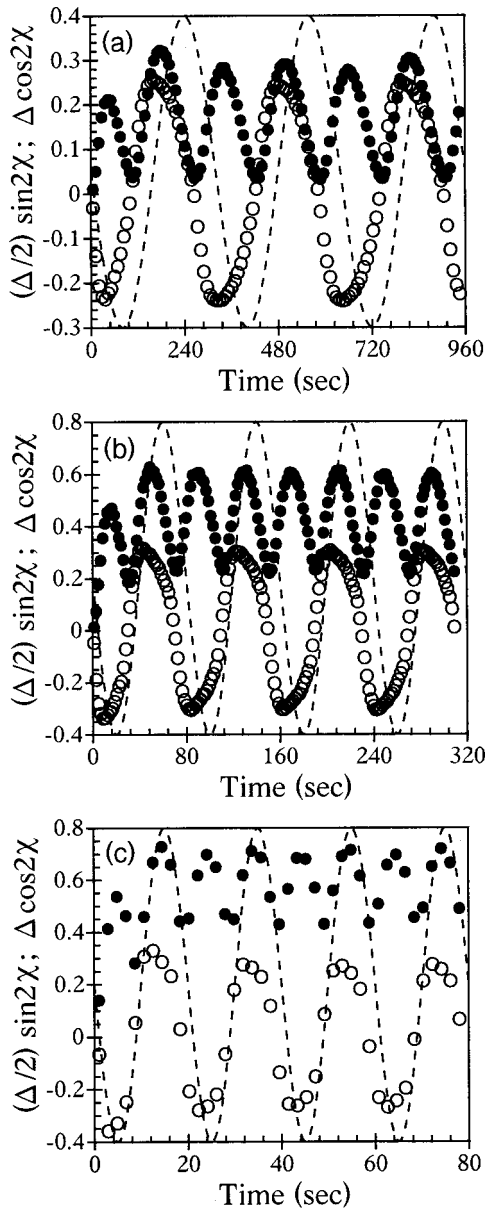


FIG. 18. Nonlinear behavior in large-amplitude oscillation: response of microemulsion structure factor to oscillatory shear deformation at 10 °C and 200% strain. X-ray shear stress analog  $\frac{1}{2}\Delta \sin 2\chi$  (○), first normal stress difference analog  $\Delta \cos 2\chi$  (●), and input strain wave (dashed curve) as a function of time. (a)  $f = 0.003\ 125$  Hz. (b)  $f = 0.0125$  Hz. (c)  $f = 0.05$  Hz.

rotated within the  $x$ - $y$  plane by the shear flow leading to the accumulation of scattered intensity along the gradient direction. We speculate that it might also be necessary to formulate theoretical models with an explicit treatment of the local interfacial structure in bicontinuous microemulsions to more accurately represent their structure and rheology under shear. Some work in this direction has been attempted [34,35].

The second major difficulty concerns the failure to find a robust stress-x-ray relation as predicted by the Pätzold and Dawson analysis. Admittedly, the second moment tensor used here to characterize x-ray anisotropy is of somewhat simpler form than the theoretical expressions for computing

stress from  $S(\mathbf{q})$ ; however, use of the full expressions does not change these conclusions [23]. There are also intrinsic limitations to the experiment (finite  $q$  range, access to only a single slice of reciprocal space) that might adversely affect prospects for confirming a stress-x-ray rule if it really did exist. If steady state data in Fig. 10 show that no stress-x-ray rule exists in this sample, the inception data on Fig. 11 demonstrate that there are still profound connections between the anisotropic structure factor and stresses in the nonlinear regime. These connections, however, seem highly dependent on the details of the transient flow. Shear flow cessation data (Fig. 13) show that x-ray anisotropy and stress relax via a very different pathway than that by which they both grow upon flow inception. It appears that fundamentally different mechanisms for stress generation exist within the microemulsion during the inception and cessation protocols, and that these mechanisms may be more subtle than the Landau-Ginzburg modeling can capture. [Experience with “stress-birefringence hysteresis” in dilute polymer solutions points out the dangers in trying to characterize complex distribution functions with low-order moments [29]; it is possible that the second moment tensor employed here may be too blunt an instrument to resolve more subtle differences in the full structure factor  $S(\mathbf{q})$  during flow inception and cessation.] Here, again, the issue of viscosity contrast in this particular sample looms large, but in the absence of a model capable of coping with this factor, it is difficult to speculate on whether there are other physical processes at play in the experiment that the model fails to capture.

The stress-x-ray failure at steady state has potential bearing on another interesting characteristic of this sample. While this paper has concentrated on nonlinear phenomena in regime II (prior to the onset of flow-induced macroscopic phase separation), the appearance of a stress plateau is another remarkable feature of this sample, which we have sought to characterize in detail [19]. Stress plateaus are frequently observed in entangled solutions of “living” worm-like surfactant micelles, and have attracted significant theoretical interest. Such plateaus have generally been interpreted in either of two ways. The first takes the stress plateau to reflect a shear banding instability due to a nonmonotonic dependence of shear stress on shear rate within a single phase material, such as would be predicted from reptation-based theories for the nonlinear rheology of entangled worm-like micelles [36]. The second takes the stress plateau to be a manifestation of a shear-induced transition from an isotropic to a nematic phase [37]. Evidence for both shear banding and shear-induced phase transitions exist in various surfactant systems, and Berret suggests that (at least in some cases) both mechanisms may act in parallel [38].

Despite the very different equilibrium structure in the microemulsion, there are strong similarities in the transient rheology we have measured in regime III [19] and the published data on surfactants. In the microemulsion case, there is compelling direct visual evidence that shear flow induces macrophase separation in regime III [17]. We hypothesize that the stress plateau in this sample is firmly connected with this phase separation. However, it is almost irresistible to point out that Pätzold and Dawson’s theory predicts a nonmono-

tonic dependence of “excess” stress on shear rate, and hence would, like the tube model, naturally predict a shear banding instability. The structural underpinnings of this nonmonotonicity are, in fact, evident in our data, where the  $x$ - $y$  component of  $\langle \hat{q}\hat{q} \rangle$  exhibits a maximum as a function of shear rate (Fig. 5). However, as seen in Fig. 10(a), stress-x-ray failure in this material means that the (background-corrected) shear stress continues to rise within regime II even after  $\langle \hat{q}_x \hat{q}_y \rangle$  has begun to decrease with increasing rate. Once within regime II, it is much harder to prove definitively whether or not a mechanical instability associated with nonmonotonic rheology in the microemulsion may play any role as a precursor to macroscopic phase separation. However, the available data suggest that, were the phase separation not to intervene, the microemulsion would by itself continue to exhibit a monotonically increasing shear stress with increasing shear rate [19].

## V. CONCLUSIONS

This study demonstrates the power of *in situ* synchrotron x-ray scattering to provide detailed information on the non-equilibrium structure factor in complex fluids under flow. Of note are (i) access to the structure factor in the flow-gradient ( $x$ - $y$ ) plane, which has provided particularly direct and useful information about shear-induced deformation and rotation of bicontinuous microemulsion structure; and (ii) high time resolution that has provided the ability to study structure development in a wide range of transient flows, and facilitated deep tests of the connection between microscopic structural changes and bulk rheology. It may be anticipated, and in some cases has been born out [22,39], that application of the annular cone and plate x-ray shear cell to other types of materials can lead to new insights into the structural origins of complicated rheology in structured fluids.

In the PEE-PDMS bicontinuous microemulsion studied here, the effects of shear on the steady state structure differ from the predictions of Pätzold and Dawson’s Landau-Ginzburg model, primarily in the strong enhancement in

scattered intensity that is observed in experiment and not predicted by the theory. We tentatively attribute this discrepancy to the model’s assumption of a uniform velocity profile at the microemulsion length scale, which appears to be inappropriate in this sample owing to high viscosity contrast between the constituents of this sample. Although no “stress-x-ray” law exists in this microemulsion system, strong connections have been found between x-ray anisotropy and stress during transient flow inception experiments. However, stress decays much more rapidly than structure factor anisotropy following flow cessation. Although the mechanical response of this sample exhibits a Rouse-like spectrum of relaxation times, the second moment tensor used to characterize anisotropy in the structure factor exhibits nearly single-exponential relaxation. A rheologically inspired phenomenological model for the second moment tensor provides essentially quantitative predictions of the structural response in step strain and oscillatory shear flow at moderate strains, although additional nonlinearity is found at higher strains.

## ACKNOWLEDGMENTS

This work was supported by the donors of the ACS Petroleum Research Fund, and through the MRSEC program of the NSF under Grant Nos. DMR-9809364 at the University of Minnesota, and DMR-0076097 at Northwestern University. X-ray experiments were conducted at the DuPont-Northwestern-Dow Collaborative Access Team (DND-CAT) Synchrotron Research Center located at Sector 5 of the Advanced Photon Source. DND-CAT is supported by the E.I. DuPont de Nemours & Co., the Dow Chemical Company, and the National Science Foundation through Grant No. DMR-9304725 and the State of Illinois through the Department of Commerce and the Board of Higher Education Grant No. IBHE HECA NWU 96. The use of the Advanced Photon Source was supported by the U.S. Department of Energy, Basic Energy Sciences, Office of Energy Research under Contract No. W-31-102-Eng-38.

- 
- [1] *Micelles, Membranes, Microemulsions and Monolayers*, edited by W. M. Gelbart, A. Ben-Shaul, and D. Roux (Springer-Verlag, New York, 1994).
- [2] G. Gompper and M. Schick, *Self-Assembling Amphiphilic Systems* (Academic, New York, 1994).
- [3] L. E. Scriven, *Nature* (London) **263**, 123 (1976).
- [4] F. S. Bates, W. W. Maurer, P. M. Lipic, M. A. Hillmyer, K. Almdal, K. Mortensen, G. H. Fredrickson, and T. P. Lodge, *Phys. Rev. Lett.* **79**, 849 (1997).
- [5] M. A. Hillmyer, W. W. Maurer, T. P. Lodge, F. S. Bates, and K. Almdal, *J. Phys. Chem. B* **103**, 4814 (1999).
- [6] T. L. Morkved, B. R. Chapman, F. S. Bates, T. P. Lodge, P. Stepanek, and K. Almdal, *Faraday Discuss.* **112**, 335 (1999).
- [7] T. L. Morkved, P. Stepanek, K. Krishnan, F. S. Bates, and T. P. Lodge, *J. Chem. Phys.* **114**, 7247 (2001).
- [8] N. Washburn, T. P. Lodge, and F. S. Bates, *J. Phys. Chem. B* **104**, 6987 (2000).
- [9] G. H. Fredrickson and F. S. Bates, *J. Polym. Sci., Part B: Polym. Phys.* **35**, 2775 (1997).
- [10] L. Corvazier, L. Messe, C. L. O. Salou, R. N. Young, J. P. A. Fairclough, and A. J. Ryan, *J. Mater. Chem.* **11**, 2864 (2001).
- [11] J. H. Lee, N. P. Balsara, R. Krishnamoorti, H. S. Jeon, and B. Hammouda, *Macromolecules* **34**, 6557 (2001).
- [12] M. Teubner and R. Strey, *J. Chem. Phys.* **87**, 3195 (1987).
- [13] G. Pätzold and K. Dawson, *J. Chem. Phys.* **104**, 5932 (1996).
- [14] G. Pätzold and K. Dawson, *Phys. Rev. E* **54**, 1669 (1996).
- [15] C.-M. Chen and G. G. Warr, *J. Phys. Chem.* **96**, 9492 (1992).
- [16] M. R. Anklam, R. K. Prud’homme, and G. G. Warr, *AIChE J.* **41**, 667 (1995).
- [17] K. Krishnan, K. Almdal, W. R. Burghardt, T. P. Lodge, and F. S. Bates, *Phys. Rev. Lett.* **87**, 098301 (2001).
- [18] K. Krishnan, B. R. Chapman, F. S. Bates, T. P. Lodge,

- K. Almdal, and W. R. Burghardt, *J. Rheol.* **46**, 529 (2002).
- [19] K. Krishnan, W. R. Burghardt, F. S. Bates, and T. P. Lodge, *Langmuir* (to be published).
- [20] W. R. Burghardt, K. Krishnan, F. S. Bates, and T. P. Lodge, *Macromolecules* **35**, 4210 (2002).
- [21] L. Noirez and A. Lapp, *Phys. Rev. Lett.* **78**, 70 (1997).
- [22] F. E. Caputo and W. R. Burghardt, *Macromolecules* **34**, 6684 (2001).
- [23] F. E. Caputo, Ph.D. thesis, Northwestern University, Evanston, Illinois, 2002.
- [24] For several shear rates, the sample was sheared in both directions. The steady state orientation angle values showed a systematic deviation between data collected in the different directions. This is manifested in Fig. 5, where the  $x$ - $y$  component of  $\langle \hat{\mathbf{q}}\hat{\mathbf{q}} \rangle$  shows two distinct values at those rates where pairs of data were collected. We attribute this to a small misalignment ( $\sim 1^\circ$ ) between the lower plate in the flow cell fixtures and the pixel array on the detector [22]. A single orientation angle correction factor was determined from all such pairs of forward/reverse steady state data, and applied after computing the orientation angle data according to Eq. (7). All orientation angle presented in this paper were so corrected. We also use the expressions  $\frac{1}{2}\Delta \sin 2\chi$  and  $\Delta \cos 2\chi$  (based on corrected  $\chi$  values) for computing the x-ray shear stress and first normal stress difference analogs, rather than using the components of the normalized second moment tensor directly.
- [25] H. Janeschitz-Kriegl, *Polymer Melt Rheology and Flow Birefringence* (Springer, Berlin, 1983).
- [26] A. Onuki and K. Kawasaki, *Ann. Phys. (N.Y.)* **121**, 456 (1979).
- [27] G. H. Fredrickson, *J. Chem. Phys.* **85**, 5306 (1986).
- [28] G. H. Fredrickson, *J. Rheol.* **38**, 1045 (1994).
- [29] P. S. Doyle, E. S. G. Shaqfeh, G. H. McKinley, and S. H. Spiegelberg, *J. Non-Newtonian Fluid Mech.* **76**, 79 (1998).
- [30] A. S. Lodge and J. Meissner, *Rheol. Acta* **11**, 351 (1972).
- [31] Note that transient viscosity measurements upon flow inception *do* suggest some strain-hardening character in the shear rheology; however, this is not manifested in step strain measurements. See Ref. [19].
- [32] R. G. Larson, *Constitutive Equations for Polymer Melts and Solutions* (Butterworths, New York, 1987).
- [33] M. H. Wagner, *Rheol. Acta* **18**, 427 (1979).
- [34] H. Kodama and S. Komura, *J. Phys. II* **7**, 7 (1997).
- [35] S. Komura and H. Kodama, *Phys. Rev. E* **55**, 1722 (1997).
- [36] N. A. Spenley, M. E. Cates, and T. C. B. McLeish, *Phys. Rev. Lett.* **71**, 939 (1993).
- [37] P. D. Olmsted, *Europhys. Lett.* **48**, 339 (1999).
- [38] J.-F. Berret, *Langmuir* **13**, 2227 (1997).
- [39] F. E. Caputo, V. M. Ugaz, W. R. Burghardt, and J.-F. Berret, *J. Rheol.* **46**, 927 (2002).